Coupling t-0 formulation with surface impedance boundary condition for eddy current crack detection

Christophe Guérin, Gérard Meunier, Fabrice Foucher

Eur. Phys. J. Appl. Phys. **52**, 23302 (2010)
DOI: 10.1051/epjap/2010061

THE EUROPEAN PHYSICAL JOURNAL APPLIED PHYSICS

Regular Article

Coupling t-ϕ formulation with surface impedance boundary condition for eddy current crack detection

C. Guérin[1,a], G. Meunier[2,b], and F. Foucher[1,c]

[1] Cedrat S.A. 15, Chemin de Malacher, 38246 Meylan Cedex, France
[2] Laboratoire de Génie Électrique de Grenoble, G2Elab, UMR 5269 INPG-UJF-CNRS, ENSIEG – BP 46, 38402 Saint-Martin-d'Hères Cedex, France

Received: 14 December 2009 / Received in final form: 18 March 2010 / Accepted: 22 March 2010
Published online: 21 October 2010 –

Abstract. We present in this paper a 3D electromagnetic formulation to describe two conductors in electric contact with each other, submitted to the field of a coil in which an AC current is flowing. One of the two conductors is described by the **t**-ϕ formulation, the other conductor is described by the surface impedance boundary condition. The proposed coupled formulation has been validated with a numerical example with a simple geometry. This coupled formulation has then been applied to a numerical example on which a crack has to be detected. It is composed of a non magnetic tube embedded in a thick steel tube sheet, submitted to the field of a coil.

1 Introduction

The finite element formulations using magnetic scalar potential ϕ and electric vector potential **t** are efficient for performing sinusoidal time variation electromagnetic simulations, i.e. magneto-harmonic simulations. It has been widely used, and presented for instance in [1–4]. An alternative to this **t**-ϕ formulation is the **A**-V formulation, where **A** is a vector potential and V an electric scalar potential [5]. We can also mention **H** or **E** field formulations [6]. For the work presented in this article, we have chosen the **t**-ϕ formulation, as we consider them as less time consuming than the other methods, and already presented our previous works about **t**-ϕ methods in [7–9], especially for the coupling with external electric circuits. **t**-ϕ formulations can describe a solid conductor in which the skin effect is not too strong. When there is a strong skin effect in a conductor, i.e. when the skin effect becomes small compared to the dimensions of the conductor, the number of elements necessary to mesh it becomes too high and it can be favourably described by the surface impedance boundary condition (IBC) [10–18]. This IBC used with the finite element method has been proposed in 2D with the magnetic vector potential **A** as state variable [10]. It has been presented in 3D with the finite element method or with the boundary integral method with the magnetic scalar potential ϕ [11–17], and with **A**-V potentials [18]. With all these methods, the conductor described with the IBC is surrounded by air and it can be in contact with a magnetic non conducting region.

The work presented in this article deals with the eddy current detection of cracks in the steam generator tubes of nuclear power plants. The tubes are embedded in a steel tube sheet and the formers are in electric contact with the latter. Each tube is submitted to the field of an emitting coil of a crack detection probe. The tube is made of Inconel (non magnetic). Cracks are present in this tube. These cracks must be detected. The skin effect is not strong in this tube. It can therefore be described by the **t**-ϕ formulation. In this article, we have considered that there is no crack in the tube sheet. As the skin effect is strong in it, it must be described by the surface impedance boundary condition. We present in this article the coupling of the **t**-ϕ formulation with the surface impedance boundary condition with an electric contact between those two conductors (the tube and the tube sheet). The proposed coupling has been validated with a numerical example with simple geometry, and has then been applied to the case of the tube embedded in the steel tube sheet. This coupling can also be applied to the simulation of other devices.

2 Numerical method

2.1 Typical problem

Let Ω_c be a conductor described by the **t**-$\mathbf{t}_0$-ϕ formulation [7–9], in electric contact with another conductor Ω_f described by the $\mathbf{t}_0$-ϕ magnetic scalar potential surface impedance formulation [11–17] (cf. Fig. 1). Let Ω_a be the

[a] e-mail: Christophe.Guerin@cedrat.com
[b] e-mail: Gerard.Meunier@g2elab.inpg.fr
[c] e-mail: Fabrice.Foucher@cedrat.com

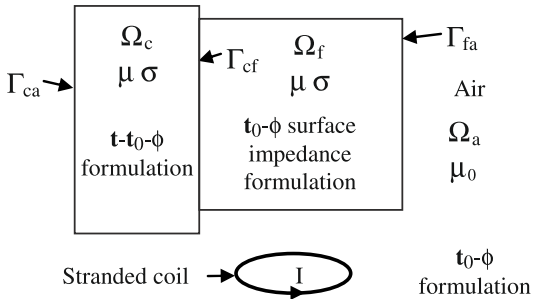

Fig. 1. Typical problem.

air region which contains a coil described by the $\mathbf{t}_0$-ϕ formulation, where $\mathbf{t}_0$ is a source magnetic field due to the current in the coil and computed as mentioned in [7–9]. Let Γ_f be the boundary of Ω_f and Γ_c, the boundary of Ω_c. Let Γ_{cf} be the interface between both conductors Ω_c and Ω_f, Γ_{fa}, the one between Ω_f and Ω_a and Γ_{ca}, the one between Ω_c and Ω_a. We then have: $\Gamma_c = \Gamma_{ca} \cup \Gamma_{cf}$ and $\Gamma_f = \Gamma_{cf} \cup \Gamma_{fa}$. Let Ω_0 be the whole finite element domain ($\Omega_0 = \Omega_a \cup \Omega_c \cup \Omega_f$) and Γ_0 its boundary. So as to clarify the presentation, we will not represent the non conducting ferromagnetic regions, as they can easily be taken into account without difficulty using $\mathbf{t}_0$-ϕ type formulations.

The source magnetic field $\mathbf{t}_0$ due to the current in the coil is defined and computed by [7–9]:

$$\begin{aligned} \mathbf{j}_s &= \mathbf{rot}\ \mathbf{t}_0 \ \text{ in } \ \Omega_0 \\ \mathbf{t}_0 \times \mathbf{n} &= 0 \ \text{ on } \ \Gamma_0 \end{aligned}$$

where $\mathbf{j}_s$ is the current density in the stranded coil. Note that the source magnetic field $\mathbf{t}_0$ is computed in the whole finite element domain Ω_0, and is also computed inside the volume of the surface impedance region Ω_f.

2.2 Surface impedance notion

When the skin depth δ becomes very small compared with the dimensions of the solid conductor regions, we can approach the solution of the problem in these regions by a monodimensional approximation along direction z, perpendicular to the surface of the conductor. We can approach $\mathbf{h}$ and $\mathbf{e}$ as follows [13]:

$$\begin{aligned} \mathbf{h}(z) &= \mathbf{h}_s e^{-\frac{(1+j)z}{\delta}} \\ \mathbf{e}(z) &= \mathbf{e}_s e^{-\frac{(1+j)z}{\delta}} \end{aligned} \tag{1}$$

where $\mathbf{h}_s$ and $\mathbf{e}_s$ are the magnetic and electric fields tangential to the Γ_f surface. The solution of the magnetoharmonic problem leads to the definition of the surface impedance Z_s [19]:

$$\begin{aligned} \mathbf{e}_s &= Z_s(\mathbf{n}_f \times \mathbf{h}_s) \\ Z_s &= \frac{1+j}{\sigma\delta}. \end{aligned} \tag{2}$$

2.3 Finite element formulation

We explain the magnetic field $\mathbf{h}$ and the current density $\mathbf{j}$ in the different regions and on the interfaces as written below:

$$\text{in } \Omega_c: \quad \mathbf{h} = \mathbf{t}_0 + \mathbf{t} - \mathbf{grad}\,\phi, \ \mathbf{j} = \mathbf{rot}\,\mathbf{t}; \tag{3}$$

$$\text{in } \Omega_a: \quad \mathbf{h} = \mathbf{t}_0 - \mathbf{grad}\,\phi; \tag{4}$$

$$\text{on } \Gamma_{fa}: \quad \mathbf{h}_s = \mathbf{t}_{0s} - \mathbf{grad}_s\,\phi; \tag{5}$$

$$\text{on } \Gamma_{cf}: \quad \mathbf{h}_s = \mathbf{t}_{0s} + \mathbf{t}_s - \mathbf{grad}_s\,\phi, \tag{6}$$

where $\mathbf{h}_s$, $\mathbf{t}_s$ and $\mathbf{t}_{0s}$ are the quantities $\mathbf{h}$, $\mathbf{t}$ and $\mathbf{t}_0$ tangential to the Γ_f interface. On Γ_{ca}, we apply the condition $\mathbf{t} \times \mathbf{n} = 0$, which ensure that $\mathbf{j} \cdot \mathbf{n} = 0$ on Γ_{ca}. With this boundary condition and the definitions (3)–(6), the $\mathbf{h}$ tangential component and the $\mathbf{j}$ normal component are conserved across interfaces. The continuities of the $\mathbf{e}$ tangential component and $\mathbf{b}$ normal component are ensured in a weak sense, i.e. by the equations to solve.

The electric field $\mathbf{e}$ and flux density $\mathbf{b}$ are expressed as function of the current density $\mathbf{j}$ and magnetic field $\mathbf{h}$ with the constitutive laws, which we write in the following form:

$$\begin{aligned} \mathbf{e} &= \rho\,\mathbf{j} = \frac{1}{\sigma}\mathbf{j} \\ \mathbf{b} &= \mu\mathbf{h} \end{aligned} \tag{7}$$

where μ is the permeability, ρ the resistivity and σ, the conductivity.

The implementation of the finite element method with the $\mathbf{t}$-$\mathbf{t}_0$-ϕ and surface impedance formulation leads to solve in a weak sense the Maxwell-Faraday and Maxwell-Gauss equations:

$$\begin{aligned} \mathbf{curl}\,\mathbf{e} &= -\frac{d\mathbf{b}}{dt} \\ \mathrm{div}\,\mathbf{b} &= 0. \end{aligned} \tag{8}$$

The Maxwell-Ampère equation is verified (strongly) by the definitions of $\mathbf{h}$ and $\mathbf{j}$ (3)–(6). To obtain the formulation, we project the above equations with adapted projection functions [20]:

$$\begin{aligned} \int_{\Omega_c} (\mathbf{curl}\,\mathbf{e} + j\omega\,\mathbf{b}) \cdot \mathbf{W}_i\, d\Omega = 0 \\ \int_{\Omega_a \cup \Omega_c} \mathrm{div}\,\mathbf{b} \cdot w_i d\Omega = 0 \end{aligned} \tag{9}$$

where $\mathbf{W}_i$ and w_i are respectively edge and nodal approximation functions. After applying Green's formulas

to these equations, we obtain:

$$\int_{\Omega_c} \mathbf{curl}\,\mathbf{W}_i \cdot \mathbf{e}\, d\Omega + \int_{\Gamma_c} (\mathbf{e} \times \mathbf{W}_i) \cdot \mathbf{n}_c\, d\Omega + j\omega \int_{\Omega_c} \mathbf{W}_i \cdot \mathbf{b}\, d\Omega = 0$$
$$\int_{\Omega_a \cup \Omega_c} \mathbf{grad}\, w_i \cdot \mathbf{b}\, d\Omega + \int_{\Gamma_f} w_i\, \mathbf{b} \cdot \mathbf{n}_f d\Omega = 0. \quad (10)$$

Where $\mathbf{n}_c$ is the normal vector pointing out of Ω_c conductor and $\mathbf{n}_f$, the normal vector pointing out of Ω_f conductor. Let us transform, in a first time, the first equation of (10), which becomes:

$$\int_{\Omega_c} \mathbf{curl}\,\mathbf{W}_i \cdot \mathbf{e}\, d\Omega + \int_{\Gamma_c} (\mathbf{n}_c \times \mathbf{e}) \cdot \mathbf{W}_i\, d\Omega + j\omega \int_{\Omega_c} \mathbf{W}_i \cdot \mathbf{b}\, d\Omega = 0. \quad (11)$$

Using the first relation of (2), noticing that $\mathbf{n}_c = -\mathbf{n}_f$ on Γ_{cf} and cancelling $\mathbf{W}_i \times \mathbf{n}_f$ on Γ_{ca}, to ensure the condition $\mathbf{j}\cdot\mathbf{n} = 0$ [21], we express the second term of (11) as follows:

$$\begin{aligned}\int_{\Gamma_{cf}} (\mathbf{n}_c \times \mathbf{e}) \cdot \mathbf{W}_i\, d\Omega &= \int_{\Gamma_{cf}} (\mathbf{n}_c \times \mathbf{e}_s) \cdot \mathbf{W}_i\, d\Omega \\ &= \int_{\Gamma_{cf}} Z_s\, (\mathbf{n}_c \times (\mathbf{n}_f \times \mathbf{h}_s)) \cdot \mathbf{W}_i\, d\Omega \\ &= \int_{\Gamma_{cf}} Z_s\, \mathbf{h}_s \cdot \mathbf{W}_i\, d\Omega. \end{aligned} \quad (12)$$

We now transform the second equation of (10). Considering the Maxwell-Faraday law in magneto-harmonic form, we can write:

$$\mathbf{b} \cdot \mathbf{n}_f = -\frac{1}{j\omega} (\mathbf{rot}\,\mathbf{e}) \cdot \mathbf{n}_f. \quad (13)$$

Using relations (2) and (13), the last term of the second equation of (10) can be transformed as follows [13]:

$$\int_{\Gamma_f} w_i \mathbf{B} \cdot \mathbf{n}_f d\Gamma = \frac{1}{j\omega} \int_{\Gamma_f} Z_s\, \mathbf{grad}\, w_i \cdot \mathbf{h}_s d\Gamma. \quad (14)$$

The system of equations to solve, obtained from the residuals (10) we have transformed, is finally in the form:

$$\int_{\Omega_c} (\mathbf{curl}\,\mathbf{W}_i \cdot \mathbf{e} + j\omega\, \mathbf{W}_i \cdot \mathbf{b})\, d\Omega + \int_{\Gamma_{c\,f}} Z_s \mathbf{W}_{s\,i} \cdot \mathbf{h}_s\, d\Gamma = 0$$
$$\int_{\Omega_a \cup \Omega_c} \mathbf{grad}\, w_i \cdot \mathbf{b} d\Omega + \frac{1}{j\omega} \int_{\Gamma_f} \mathbf{Z}_s\, \mathbf{grad}_s w_i \cdot \mathbf{h}_s\, d\Gamma = 0. \quad (15)$$

We interpolate ϕ and $\mathbf{t}$ on the finite element mesh with shape functions identical to the projection functions:

$$\mathbf{t} = \sum_j \mathbf{W}_j t_j$$
$$\phi = \sum_j w_j \phi_j$$

where the t_j and ϕ_j are the unknowns of the system to solve [7–9,12].

The symmetry of the system is obtained multiplying the second equation of (15) by $j\omega$. We then obtain the following system of equations, in the case of natural boundary conditions:

$$\begin{bmatrix} A & B \\ B^t & C \end{bmatrix} \begin{Bmatrix} t \\ \phi \end{Bmatrix} = \begin{Bmatrix} D \\ E \end{Bmatrix} \quad (16)$$

$$A_{ij} = \int_{\Omega_c} \rho\, \mathbf{curl}\,\mathbf{W}_i \cdot \mathbf{curl}\,\mathbf{W}_j\, d\Omega + j\omega \int_{\Omega_c} \mu\, \mathbf{W}_i \cdot \mathbf{W}_j\, d\Omega + \int_{\Gamma_{c\,f}} Z_s\, \mathbf{W}_{s\,i} \cdot \mathbf{W}_{s\,j}\, d\Gamma$$
$$B_{ij} = -j\omega \int_{\Omega_c} \mu\, \mathbf{W}_i \cdot \mathbf{grad}\, w_j d\Omega - \int_{\Gamma_{c\,f}} Z_s\, \mathbf{W}_{s\,i} \cdot \mathbf{grad}_s\, w_j\, d\Gamma$$
$$C_{ij} = j\omega \int_{\Omega_a \cup \Omega_c} \mu\, \mathbf{grad}\, w_i \cdot \mathbf{grad}\, w_j\, d\Omega + \int_{\Gamma_f} Z_s\, \mathbf{grad}_s\, w_i \cdot \mathbf{grad}_s\, w_j\, d\Gamma$$
$$D_i = -\int_{\Gamma_{c\,f}} Z_s \mathbf{W}_{s\,i} \cdot \mathbf{t}_{0s}\, d\Gamma$$
$$E_i = j\omega \int_{\Omega_a} \mathbf{grad}\, w_i \cdot \mathbf{t}_0 d\Omega + \int_{\Gamma_{f\,a}} Z_s\, \mathbf{grad}_s w_i \cdot \mathbf{t}_{0s}\, d\Gamma.$$

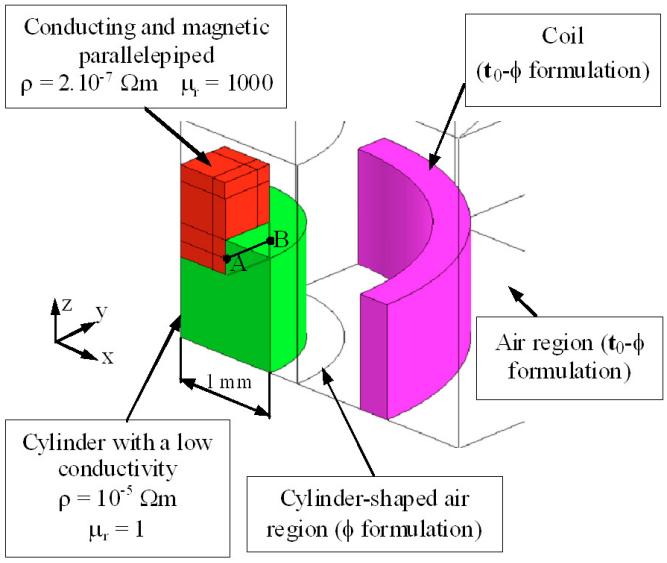

Fig. 2. (Color online) Geometry description of the example. With the 3 symmetries, one eighth of the geometry is described.

The system of equations (16) corresponds to the "reduced" scalar potential formulation ($\mathbf{t}_0$-ϕ or $\mathbf{t}$-$\mathbf{t}_0$-ϕ). The "total" scalar potential formulation, i.e. the ϕ or $\mathbf{t}$-ϕ formulation, can be obtained cancelling D and E terms of (16). We can have, in the same problem, conducting or non conducting regions described by a "reduced" scalar potential formulation ($\mathbf{t}_0$-ϕ or $\mathbf{t}$-$\mathbf{t}_0$-ϕ) and others described with the "total" scalar potential formulation (ϕ or $\mathbf{t}$-ϕ). It is also possible to describe a part of the couple of conductors $\Omega_c \cup \Omega_f$ with "total" scalar potential formulations and another one with "reduced" scalar potential formulations.

We have used the tree-cotree gauge applied to the electric vector potential $\mathbf{t}$ [22], where the unknowns t_i are cancelled on the edges of a tree spanning the Ω_c conductor described by the $\mathbf{t}$-$\mathbf{t}_0$-ϕ or $\mathbf{t}$-ϕ formulation. The linear system solving algorithm used is a preconditioned conjugate gradient algorithm after equilibrating the linear system [23]. The coupling method presented in this part has been implemented in the Flux® software [24].

3 Simple geometry numerical example for the validation

3.1 Description of the numerical example

We have validated the coupling presented above on a simple geometry example composed of a magnetic parallelepiped conductor inserted in a non magnetic cylinder-shaped conductor with a low conductivity (cf. Fig. 2). A coil in which flows a sinusoidal current at a frequency equals to 10 kHz, 100 kHz or 1 MHz generates induced currents in both conductors which are in electric contact with each other: the cylinder-shaped conductor and the parallelepiped conductor.

Table 1 gives the values of the skin depth in these 2 conductors, at the 3 frequencies of the coil current. The

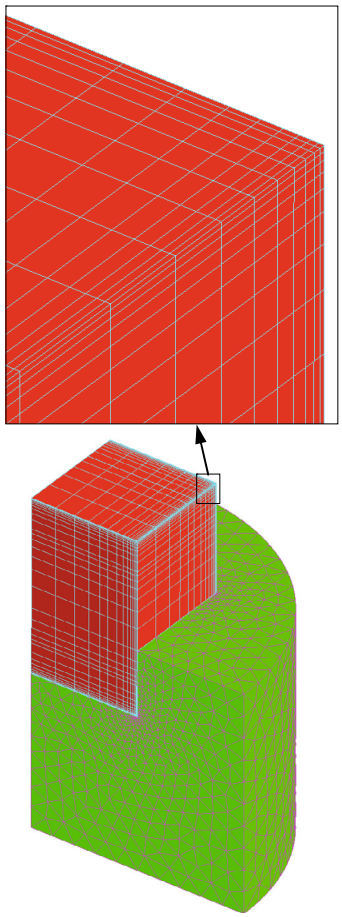

Fig. 3. (Color online) Mesh of both conductors.

Table 1. Skin depths in both conductors for the 3 frequencies of current in the coil.

Frequency	Parallelepiped conductor	Cylinder-shaped conductor
10 kHz	0.071 mm	16 mm
100 kHz	0.022 mm	5.0 mm
1 MHz	0.0071 mm	1.6 mm

cylinder-shaped conductor, in which skin depth is between 1.6 mm and 16 mm, is described by the $\mathbf{t}$-ϕ formulation. In the parallelepiped conductor, skin depth is between 0.0071 mm and 0.071 mm. For each frequency, two simulations have been performed:

- 1st case, the parallelepiped conductor is described by the ϕ surface impedance formulation, using the method described above;
- 2nd case, considered as the reference case, this conductor is described by the $\mathbf{t}$-ϕ formulation.

In both cases, a cylindrical air region including the 2 conductors (which can be seen in Fig. 2) is described by the ϕ formulation. The region which consists of the rest of air and the coil are described by the $\mathbf{t}_0$-ϕ formulation.

In Figure 3 is depicted the mesh used for a frequency equal to 1 MHz. The parallelepiped conductor has been meshed with hexahedral finite elements. On the edges, the

Table 2. Eddy current losses in the parallelepiped conductor.

Frequency	1st case	2nd case	Difference
10 kHz	6.92×10^{-8} W	6.73×10^{-8} W	2.81%
100 kHz	2.11×10^{-6} W	2.09×10^{-6} W	0.756%
1 MHz	5.84×10^{-5} W	5.76×10^{-5} W	1.47%

Table 3. Eddy current losses in the cylinder-shaped conductor.

Frequency	1st case	2nd case	Difference
10 kHz	1.99×10^{-8} W	2.01×10^{-8} W	0.82%
100 kHz	1.951×10^{-6} W	1.956×10^{-6} W	0.24%
1 MHz	1.804×10^{-4} W	1.805×10^{-4} W	0.071%

elements are very elongated and have a width equal to 0.002 mm, so the mesh is compatible with the skin depth of 0.0071 mm at this frequency.

3.2 Results

The convergence of the linear system is always obtained. Tables 2 and 3 and Figures 4–7 show that the method presented in this article gives good results.

In Figure 4, on the vertical edge of the parallelepiped conductor, the current density is very small in the 2nd case and not in the 1st case. We can explain that with the following considerations: in the 2nd case, the parallelepiped conductor is described with the **t**-ϕ formulation, it is much more conducting than the cylinder-shaped conductor, the current density passes from a vertical face to the other passing through the interior of the volume, so the current density is taking the shortest way. The higher the frequency is, the smaller the skin depth is and the smaller the zone with very small current density on the vertical edge is. In the 1st case, the current density is not small on the edge, because it is tangential to each face, since the surface impedance formulation imposes that the current density be tangential to the surface of the conductor. In Table 2, we can see that the difference at 1 MHz is increased compared with the one at 100 kHz. It is probably due to a not enough refined mesh for the second case at this frequency.

Figures 6 and 7 show curves of the current density and flux density, calculated on the AB segment, located at the interface between the parallelepiped conductor and the cylinder-shaped conductor in both cases (AB segment is depicted in Fig. 2). Figure 6 shows curves of the imaginary part of the y-component of the current density **j** in the parallelepiped conductor at 100 kHz. The y-component of the current density **j** is the highest of the 3 components and **j** is tangential to the AB segment. We notice a small difference of values between both cases. At abscissa 0.5 mm, corresponding to the vertical edge of the parallelepiped conductor, the current density is very small in the 2nd case. We find again the phenomenon already observed in Figure 4 and which we have already explained above. Figure 7 shows the curves of the real part of the z-component

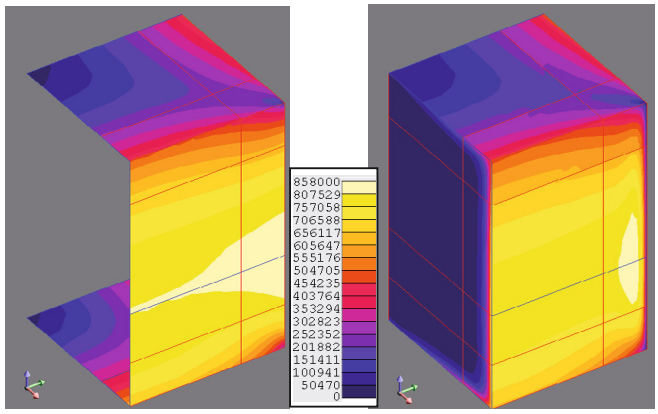

Fig. 4. (Color online) Isovalues of the current density modulus in the parallelepiped conductor, at 100 kHz: on the left 1st case (with parallelepiped conductor described with the surface impedance formulation), on the right 2nd case (with parallelepiped conductor described with the **t**-ϕ formulation). The scale of the current density is in A/m^2.

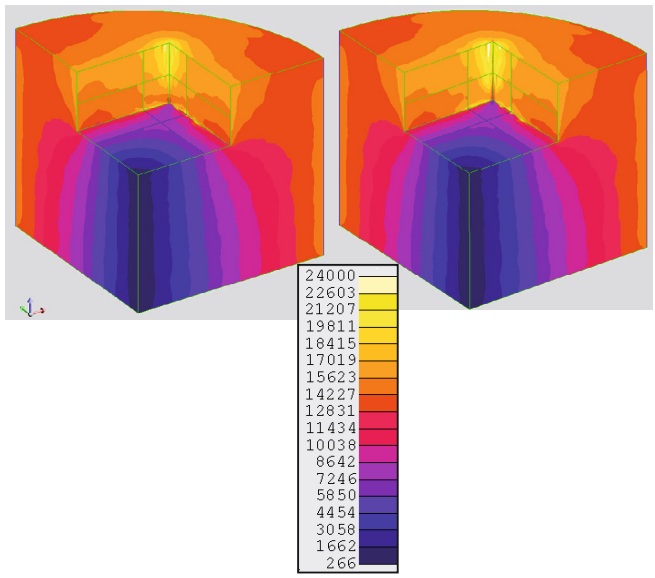

Fig. 5. (Color online) Isovalues of the current density modulus in the cylinder-shaped conductor, at 100 kHz: on the left 1st case (with parallelepiped conductor described with the surface impedance formulation), on the right 2nd case (with parallelepiped conductor described with the **t**-ϕ formulation). The scale of the current density is in A/m^2.

of the flux density **b** in the cylinder-shaped conductor at 100 kHz. The real part of this z-component is the highest of the 3 components. The curves of the imaginary part of the z-component show the same shapes. We observe that the curves corresponding to both cases are superimposed, which shows that the surface impedance formulation, even if it is not accurate near the vertical edge does not modify very much the results in the cylinder-shaped conductor described by the **t**-ϕ formulation. In Figure 7, close to abscissa 0.5 mm, corresponding to the vertical edge, the curve presents oscillations, which would probably be due to the mesh which is not enough fine in this area.

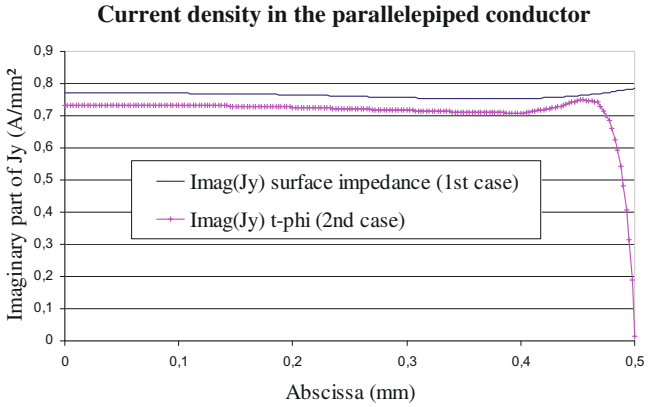

Fig. 6. (Color online) Curves of the imaginary part of the y-component of the current density $\mathbf{j}$ in the parallelepiped conductor, on the AB segment, at 100 kHz, in both cases.

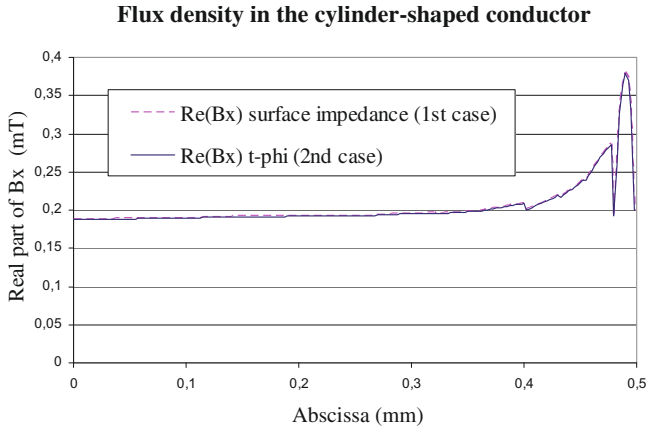

Fig. 7. (Color online) Curves of the real part of the x-component of flux density $\mathbf{b}$ in the cylinder-shaped conductor, on the AB segment, at 100 kHz, in both cases.

4 Numerical example of a tube with crack embedded in a tube sheet

4.1 Description of the numerical example

We have then used the method presented above on a device which comprises a steam generator tube embedded in a steel tube sheet. The tube contains a crack and is submitted to the field of an emitting coil of a crack detection probe.

In the steam generators, the tubes made of Inconel (non magnetic) of around 22 mm diameter are embedded in a 30 mm thick steel tube sheet and expanded. The tubes and the tube sheet are in electric contact. Each tube is submitted to the field of an emitting coil of a crack detection probe. The numerical example we have simulated is composed of a part of tube embedded in a part of the tube sheet. The tube has a larger diameter in the lower part than in the upper part. In the upper part, the diameter of the tube is equal to 19.7 mm, whereas in the lower part, its diameter is equal to 20.4 mm. There is a zone where the tube is cone-shaped. The tube is submitted to

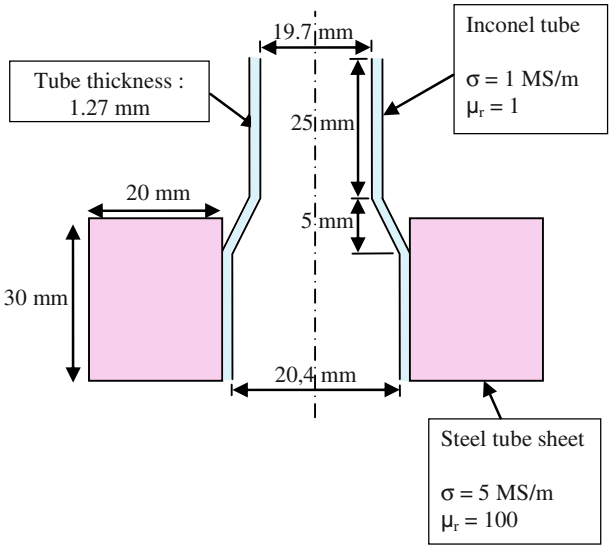

Fig. 8. (Color online) Geometry of the tube and tube sheet, with material properties indicated.

Table 4. Skin depths in the tube and the tube sheet for the 2 working frequencies of the probe.

Frequency	Tube	Tube sheet
100 kHz	1.6 mm	0.071 mm
600 kHz	0.65 mm	0.029 mm

the magnetic field of the probe emitting coil. In this example, we have placed this latter in the cone-shaped zone of the tube and the rest of the probe (receiving coils, ferrite) are not represented. We have described only one fourth of the device with two vertical symmetry planes. On the first plane which cuts the coil, we have imposed a tangential magnetic field boundary condition. We suppose that the field of the coil is negligible in the diametrically opposite zone (see Fig. 9). Thanks to this approximation, the second vertical symmetry plane was put to reduce the number of nodes of the problem. In Figure 8, we give the main dimensions taken for the simulation, for the tube and tube sheet, as well as the used material characteristics. It is necessary to model the tube sheet as it modifies the probe response. Indeed, the impedance measured by the probe receiving coils is not the same when this probe is in the lower part or in the upper part of the tube.

Table 4 gives the values of skin depths in the tube and tube sheet at working frequencies of the probe: 100 kHz and 600 kHz. At these frequencies, skin depth is much smaller than the dimensions of the tube sheet, which means that the use of the surface impedance boundary condition in this region is valid. In the tube, the mesh consists of 8 layers of hexahedral elements (cf. Fig. 10).

The tube is described by the $\mathbf{t}$-ϕ formulation and the tube sheet by the ϕ surface impedance formulation, using the method described in this article. The air region surrounding the coil inside the tube is described by the $\mathbf{t}_0$-ϕ formulation. The rest of the air region is described by the ϕ formulation.

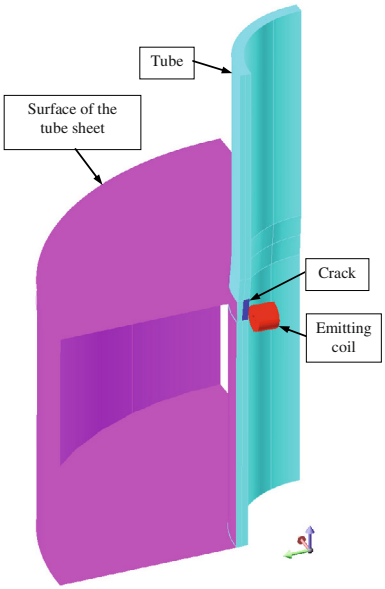

Fig. 9. (Color online) Geometry described for the simulation.

We have performed 2 computations, one, without crack, the other with a crack. It is situated on the symmetry plane which cuts the coil, in the cone-shaped zone of the tube, and is 2.5 mm high, and has a depth half the one of the tube (cf. Fig. 9). We have described the crack by a $\mathbf{t} \times \mathbf{n} = 0$ boundary condition on a nearly rectangular face, which imposes a zero normal component of current density $\mathbf{j}$ on this face. This boundary condition describes a perfectly insulating surface crack. It is quite possible to describe an insulating volume crack, for instance: a parallelepiped crack. On the example, we have performed the simulations at 600 kHz frequency, which corresponds to the most difficult simulation in terms of convergence of the linear system solving algorithm and in terms of computation time, because the skin depths are the smallest and the numbers of finite elements and unknowns are the highest.

4.2 Results

Without the tree-cotree gauge applied to the electric vector potential $\mathbf{t}$, the example of the tube embedded in the tube sheet does not converge at the 600 kHz frequency. In Figures 11 and 12 are represented the arrows and isovalues of the current density in the tube, in the case "without crack" and "with crack". In the case "with a crack", the current flows under the crack and is therefore more important on the external face of the tube, on the tube sheet side.

In Figure 13 are represented the arrows of the current density $\mathbf{j}$ on the tube sheet, in the case "with crack". The arrows of the case "without crack" are not represented because they are a lot alike those represented in Figure 13.

In Figure 14 are represented the isovalues of the current density $\mathbf{j}$ in the tube sheet, in the case "without crack" and "with crack". The current density in the tube sheet is a little more greater in the case "with crack" than in the case "without crack", as we can see it in Figure 14, although the maximum values between both cases are very close. This can be explained by the crack which forces currents to pass under the crack, therefore to be closer to the surface of the tube sheet than in the case "without crack".

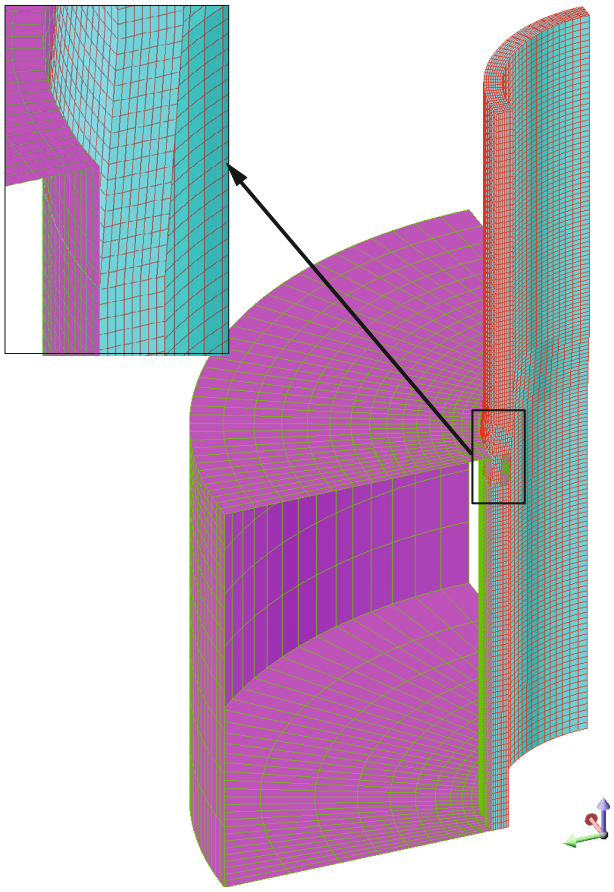

Fig. 10. (Color online) Mesh of the tube and surface of the tube sheet, with a zoom of the cone-shaped zone of the tube.

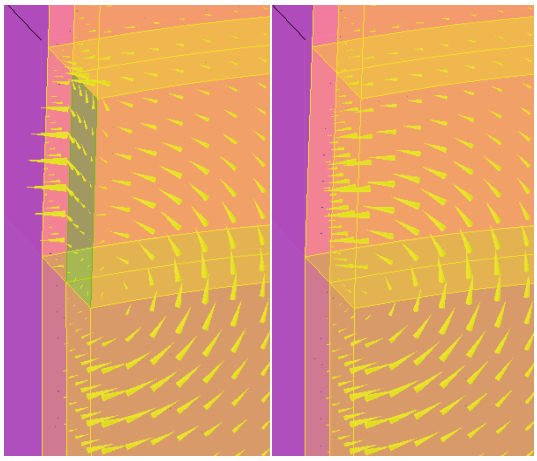

Fig. 11. (Color online) Arrows of the current density in the tube, under the coil, for $\omega t = 120°$: on the left, in the case "with a crack", on the right, in the case "without crack".

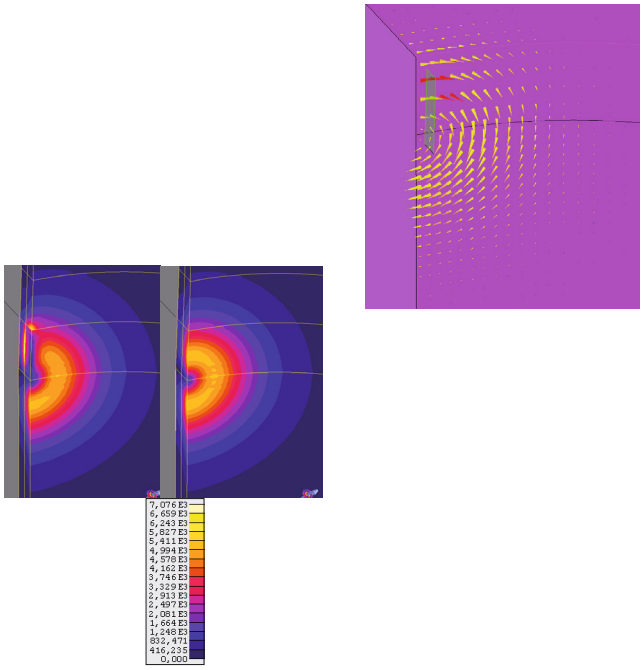

Fig. 12. (Color online) Isovalues of the current density modulus in the tube, under the coil: on the left, in the case "with a crack", on the right, in the case "without crack". The scale of the current density is in A/m^2.

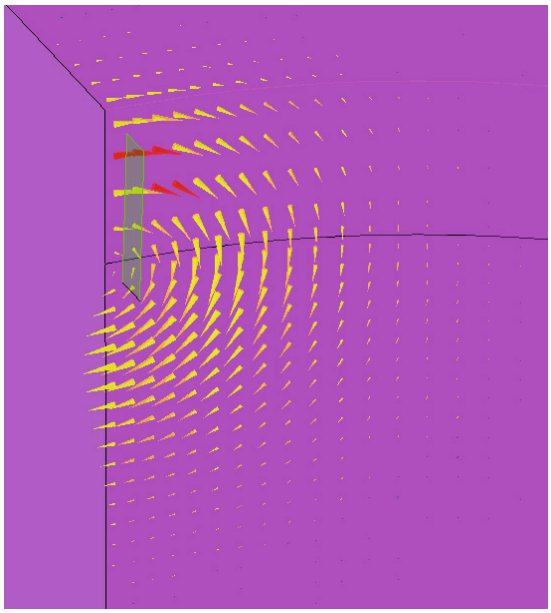

Fig. 13. (Color online) Isovalues of the surface current density on the surface of the tube sheet, under the coil, in the case "with a crack", for $\omega t = 90°$.

5 Conclusion

We have developed and validated a method which allows to model a conductor described by the **t**-ϕ formulation in electric contact with another one described by the surface impedance boundary condition. The coupling presented in this article has been validated with a numerical example

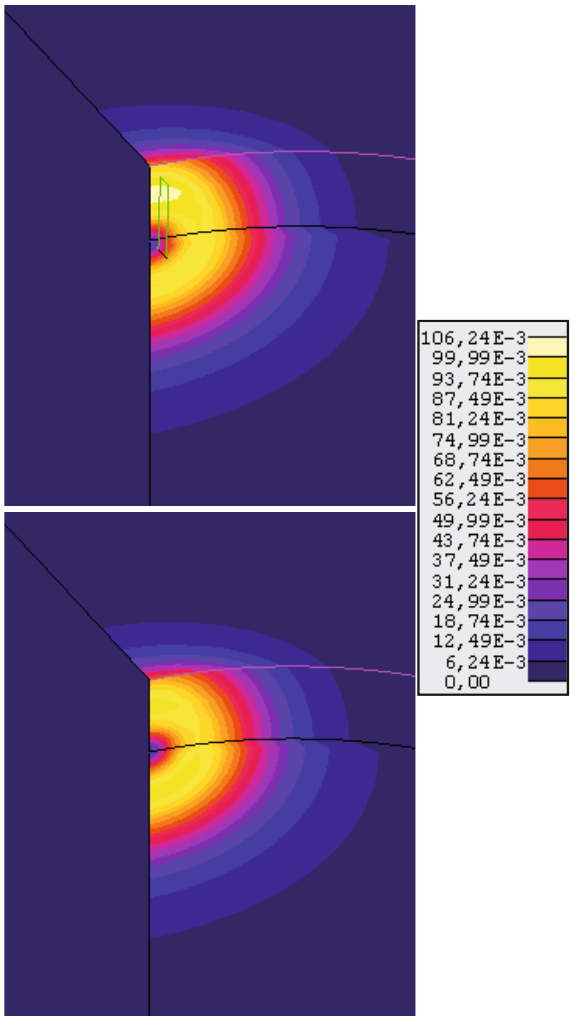

Fig. 14. (Color online) Isovalues of the surface current density on the surface of the tube sheet, under the coil: at the top, in the case "with a crack", at the bottom, in the case "without crack". The scale of surface current density is in A/m.

of simple geometry. This coupling has then been applied to a crack detection problem in steam generators. This problem consists of a non magnetic tube embedded in a steel tube sheet, submitted to the field of an emitting coil of a crack detection probe. Future work will deal with the extension of the coupling method to the couples of multiply connected conductors, i.e. with holes, and coupled with an external electric circuit. The same approach will also be developed with the **A**V-**A** formulation [18]. It will be possible to model a conductor described by the **A**-V formulation in electric contact with another one described by the surface impedance boundary condition with **A**-V potentials.

This work has been carried out as part of the ANR "Playa" project for the promotion of the simulation of eddy current Non Destructive Testing processes.

References

1. T.W. Preston, A.B.J. Reece, IEEE Trans. Magn. **18**, 486 (1982)
2. T. Nakata, N. Takahashi, K. Fujiwara, Y. Okada, IEEE Trans. Magn. **24**, 94 (1988)
3. F. Bouillaut, Z. Ren, A. Razek, IEEE Trans. Magn. **26**, 478 (1990)
4. J.P. Webb, B. Forghani, Proc. IEE Sci. Meas. Technol. **142**, 133 (1995)
5. O. Biro, K. Preis, IEEE Trans. Magn. **25**, 3145 (1989)
6. A. Bossavit, IEEE Trans. Magn. **24**, 74 (1988)
7. Y. Le Floch, Ph.D. thesis, Institut National Polytechnique de Grenoble (INPG), 2002
8. G. Meunier, Y. Le Floch, C. Guérin, IEEE Trans. Magn. **39**, 1729 (2003)
9. G. Meunier, Y. Le Floch, C. Guérin, RIGE **8**, 9 (2005)
10. S.R.H. Hoole, C.J. Carpenter, IEEE Trans. Magn. **21**, 1841 (1985)
11. G. Tanneau, IEEE Trans. Magn. **24**, 467 (1988)
12. D. Rodger, P.J. Leonard, H.C. Lai, R.J. Hill-Cottingham, IEEE Trans. Magn. **27**, 4995 (1991)
13. C. Guérin, Ph.D. thesis, Institut National Polytechnique de Grenoble (INPG), 1994
14. C. Guérin, G. Meunier, G. Tanneau, IEEE Trans. Magn. **32,** 808 (1996)
15. L. Krähenbühl, O. Fabrègue, S. Wanser, M. De Sousa Dias, A. Nicolas, IEEE Trans. Magn. **33**, 1167 (1997)
16. G. Meunier, Y. Le Floch, C. Guérin, COMPEL **27**, 64 (2008)
17. C. Guérin, G. Meunier, Y. Le Floch, RIGE **11**, 149 (2008)
18. F.-Z. Louai, D. Benzerga, M. Feliachi, F. Bouillault, IEEE Trans. Magn. **32**, 812 (1996)
19. R.L. Stoll, *The analysis of eddy currents* (Clarendon Press, Oxford, 1974)
20. P. Dular, F. Piriou, in *Modèles et formulations en électromagnétisme, Traité EGEM* (Hermès Science, Lavoisier, 2002)
21. A. Bossavit, EDF R&D, Clamart, Report No. HI70/6284, 1989
22. R. Albanese, G. Rubinacci, Int. J. Num. Meth. Eng. **29**, 453 (1990)
23. C. Doucet, I. Charpentier, J.L. Coulomb, C. Guérin, Y. Le Floch, G. Meunier, COMPEL **27**, 897 (2008)
24. Flux®, Cedrat, www.cedrat.com